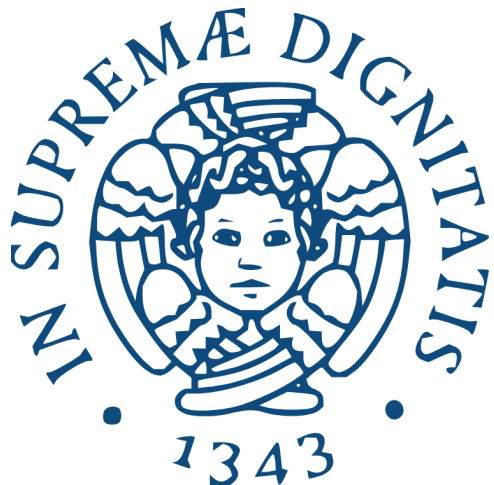


University of Pisa



Laboratory Report

Spectral Analysis of Vega and Jupiter with Determination of Jupiter's Rotation Period via Sodium Doublet Doppler Shift

Professors:

Prof. Massimiliano Razzano
Prof. Angelo Ricciardone
Prof. Barbara Patricelli
Prof. Andrea Pallottini

Candidates:

Nicolò Aimone Braida (701844)
Matilde Biscaro (702943)
Lorenzo Nepi (701845)

Abstract

Astronomical spectroscopy allows us to investigate the physical and kinematic properties of celestial bodies through the analysis of their spectra. The aim of this study is to identify the NaI doublet lines (5890 Å and 5896 Å) in the spectra of Vega and Jupiter, and to determine the rotational velocity of the planet using spectroscopic data obtained with the Lhires spectrograph. In the first part of the analysis, the scientific frames were processed and calibrated, and the spectra were extracted. The NaI D2 line was clearly identified in the Vega spectrum, while the D1 line could not be distinguished due to its low intensity and the noise level. In the second part, the kinematic properties of Jupiter were inferred from the Doppler shift of the NaI doublet. We determined a radial velocity of -3.0 ± 2.5 km/s, an equatorial rotational velocity of 11.0 ± 2.5 km/s and a rotational period of 11.4 ± 2.6 hours. These results are consistent with values reported in the literature. Finally, we discuss the main sources of uncertainty affecting our measurements.

Contents

1	Introduction	1	to identify the flux as a function of wavelength. Spectra can be classified into three types: continuous spectrum, emission spectrum, and absorption spectrum.
2	Theoretical Background	1	The analysis of the spectra of astronomical objects allows us to derive a number of important properties of the sources of radiation, as briefly summarized below:
2.1	The atomic structure	2	1. temperature and excitation state;
2.2	NaI D doublet	2	2. pressure or density;
2.3	Line Broadening	2	3. chemical composition;
2.4	Spectral classification of stars	3	4. radial velocities and velocity fields (kinematics, at the basis of mass studies);
2.5	Doppler Effect	3	5. strength of magnetic fields.
3	Instrumental set-up	3	
3.1	The Lhires III	4	
4	Observation and Data Collection	4	
5	Data Reduction and Results	5	The aim of this work is to analyze the spectra of Vega and Jupiter obtained with the Lhires (Littrow High Resolution Spectrograph), and to infer the kinematics of a rotating body through the observation of an emission line.
5.1	Spectrum Reduction	5	Let us start with the description of the physical mechanisms at the base of the spectroscopic data analysis.
5.2	Spectral Alignment	6	Then, we present the instrumentation and explain how
5.3	Sky subtraction	7	the observations were conducted. Subsequently, we process the scientific images using calibration frames, align
5.4	Spectrum extraction	7	the spectra, and calibrate them in wavelength, converting pixel positions into physical wavelength units.
5.5	Wavelength Calibration	7	Once the spectra are calibrated, we proceed with the analysis,
5.6	Spectral Resolution and binning error . . .	8	identifying the absorption lines of the sodium NaI doublet and extracting information about Jupiter's kinematics and calculating its rotational period.
5.7	Spectral analysis of Vega	8	Throughout the analysis, we also examine the resolution of the spectrograph and discuss the main sources of error and
5.8	Spectral analysis of Jupiter: radial velocity	10	difficulties encountered during the data reduction and interpretation.
5.9	Spectral Analysis of Jupiter: Rotational Period	10	
6	Discussion	11	
7	Conclusion	12	
A	Figures	13	
B	References	14	

1 Introduction

Spectroscopy is an astronomical observation technique based on the dispersion of light from a source, which is employed

2 Theoretical Background

In this section, we provide a brief theoretical overview of the physical principles that we will apply in the following

sections to derive the physical quantities of interest, such as the radial velocities of the targets and the rotational period of Jupiter, from the spectroscopic data collected.

2.1 The atomic structure

The discrete energy-level-structure of an atom and the motion of the electrons is characterized by four quantum numbers: the *principal quantum number* n , which refers to the quantization of the energy levels, the *orbital quantum number* ℓ , which is related to the angular momentum of the orbits and their eccentricity, the *magnetic quantum number* m , which characterizes the component of the angular momentum vector along a preferred direction and the *spin quantum number*, which defines an intrinsic angular momentum of the electrons along a preferred direction. These four quantum numbers characterize single-particle states called *orbitals*.

The full treatment of the energy of the electrons in an atom also requires considering the electrostatic repulsion between the electrons and the spin-orbit interaction. This is addressed using the so-called *LS coupling scheme*, which evaluates these two additional contributions separately. The energy contribution from the electron-electron pair repulsion yields an energy splitting of the configurations into *terms*, which are characterized by the quantities $\mathbf{L} = \sum_i \ell_i$ and $\mathbf{S} = \sum_i \mathbf{s}_i$, where the sums are vectorial sums. Then, the spin-orbit interaction introduces a further splitting into additional energy *levels*, which depends on the sum of the $\ell_i \cdot \mathbf{s}_i$ quantities over all electrons. In *LS coupling* scheme the energy contribution from the spin-orbit interaction depends on the total angular momentum vector $\mathbf{J} = \mathbf{L} + \mathbf{S}$. A *level* is specified by the L , S values, the parity π , and the total angular momentum J

$$2S+1 L_J^\pi$$

where the possible values J are $J = L + S, \dots, |L - S|$. In spectroscopic notation the total angular momentum is represented with upper case letters:

total angular momentum:	S	P	D	F	G
$L =$	0	1	2	3	4

In calculating the value of L one considers all possible combinations of the ℓ values for the valence electrons. The shift in energy between different values of the corresponding quantum number J is small compared to the energy differences between *terms* and gives rise to the so-called *fine structure* of the energy levels. Transitions between *levels* result in spectral lines, while transitions between *terms* give rise to *multiplets* (an ensemble of lines). A *resonance line* corresponds to the transition between the first allowed excited level and the ground state.

2.2 NaI D doublet

Sodium is an alkali metal with a ground state configuration $1s^2 2s^2 2p^6 3s$ thus the corresponding term is ${}^2S_{1/2}$ ($L = 0$, $S = 1/2$). A partial Grotrian diagram is shown in Fig. 1. In the first excited state the single valence

electron is moved to $3p$. The correspondent term 2P is split by spin-orbit interaction into two levels, separated by 2.1×10^{-3} eV: ${}^2P_{3/2}$ ($L = 1$, $S = 1/2$, $J = 3/2$) and ${}^2P_{1/2}$ ($L = 1$, $S = 1/2$, $J = 1/2$). The first configuration is more energetic than the second (consult <https://www.nist.gov/pml/atomic-spectra-database>). The NaI D doublet at the wavelengths of 5890 Å and 5896 Å is the *resonance line* produced by the transitions ${}^2S_{1/2} - {}^2P_{1/2}$ (D_1 line at 5896 Å) and ${}^2S_{1/2} - {}^2P_{3/2}$ (D_2 line at 5890 Å)¹. The D doublet is observed in absorption in the interstellar medium of galaxies and in solar-type stars.

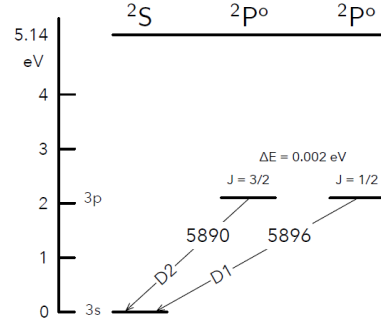


Figure 1: Partial Grotrian diagram for NaI, showing the transitions corresponding to the D doublet.

2.3 Line Broadening

Absorption and emission from isolated spectral lines cover a finite frequency (or wavelength) range. This happens because different broadening mechanisms act on the spectral lines. The principal broadening mechanisms are the following:

- *Natural broadening*, which arises from the quantum-mechanical uncertainty in the energies of the quantum states involved in the transition. The resulting line profile, centered at frequency ν_0 , follows a Lorentzian distribution. However, the natural width of most spectral lines is extremely narrow, so other broadening mechanisms typically dominate.
- *Instrumental broadening*, caused by the finite spectral resolution of the spectrometer. This imposes an instrumental profile on any infinitely narrow line, and this profile is often convolved with other broadening effects.
- *Rotational broadening*, resulting from the Doppler effect due to source rotation. If the source rotates around an axis, that is inclined with respect to the observer's line of sight, some parts of the surface move toward the observer while others move away, introducing a distribution of radial velocities that broadens the spectral lines.
- *Thermal broadening*, due to the microscopic motion of atoms and molecules. The thermal velocity distribution increases with temperature and decreases with particle mass. This motion induces Doppler shifts that broaden the spectral lines, producing a Gaussian profile.

¹The D₁, D₂ nomenclature originates from Fraunhofer's spectrum of the Sun.

- *Microturbulence*, which refers to small-scale turbulent motions, such as those caused by convective flows in a star's atmosphere. Like thermal broadening, microturbulence introduces relative motion among emitting or absorbing regions, also resulting in a Gaussian line profile.
- *Pressure broadening*, often the dominant broadening mechanism in the outer wings of stellar spectral lines. It is caused by perturbations of atomic energy levels due to interactions with nearby charged particles, particularly with free electrons. This interaction figures out in a Lorentzian profile.

When we consider together the different mechanisms responsible for line broadening, the Gaussian profile dominates in the line center, while the Lorentzian profile dominates in the line wings. The resulting line shape is described by the Voigt profile, which is the convolution of a Gaussian and a Lorentzian function.

2.4 Spectral classification of stars

Astronomers classify stars based on the relative strength of their absorption lines. The spectral classification scheme currently in use was developed at the Harvard Observatory in the United States in the early 20th century. It is primarily based on spectral lines that are sensitive to stellar temperature, rather than to surface gravity or luminosity. The main spectral types in the Harvard classification are denoted by capital letters: O, B, A, F, G, K, and M. Each spectral type is further divided into ten subclasses, numbered from 0 to 9. Stars exhibit various patterns of absorption lines, among which the Balmer series of hydrogen is particularly important. Other significant spectral features include lines from atoms such as calcium (Ca), iron (Fe), and sodium (Na), as well as molecular bands from compounds such as titanium oxide (TiO) and magnesium hydride (MgH).

In the following sections, we will analyze the spectra of Vega and the Sun, reflected by Jupiter. These stars exhibit the following characteristics:

- Vega is classified as an A0-type star. A-type stars are white stars with surface temperatures of approximately 9000 K. In this spectral class, hydrogen Balmer (HI) lines are very strong and dominate the spectrum, while they gradually weaken in later types while calcium (CaII) lines become more prominent. Helium (HeI) lines are not visible, and neutral metal lines are present. In the spectrum of Vega, the NaI doublet appears weak but detectable.
- The Sun is classified as a G2-type star. G-type stars are yellow stars with surface temperatures around 5500 K. In this class, HI lines are relatively weak, while metal lines are strong. The NaI doublet is a strong line in the solar spectrum.

2.5 Doppler Effect

Doppler effect is a wavelength-shift between emitted light and received light when the object and the observer are in relative motion. If they approach themselves, the shift

is toward the blue; if they are moving away, it is toward the red. The Doppler effect formula is the following:

$$\frac{\lambda_{oss} - \lambda_{lab}}{\lambda_{lab}} \approx \frac{v}{c} \quad (1)$$

where c indicates the speed of light in the vacuum, v is the relative velocity, λ_{lab} is the wavelength at which a certain line is observed from a frame of reference comoving with the system that emitted such line (the so called *laboratory frame*), while λ_{oss} refers to the wavelength at which the line is actually observed as a consequence of a Doppler shift. Equation 1 is valid only for non-relativistic speeds.

The Doppler effect enables the measurement of radial velocity, rotational speed, and expansion velocity by analyzing emission and absorption lines. In Section 5.8, assuming solid body rotation and adopting the far-source approximation², we derive the rotational period of Jupiter from the tilt observed in its spectral lines. As shown in Fig. 2, the limb of the planet rotating toward the observer exhibits a blueshift, while the opposite limb, moving away, is redshifted. This Doppler shift is directly proportional to the radial component of the rotational velocity, resulting in a measurable tilt of the spectral lines. The tangential velocity can therefore be determined by measuring the wavelength displacement $\Delta\lambda$ and applying the Doppler effect formula:

$$v_r = \frac{1}{4} \frac{\Delta\lambda}{\lambda_{lab}} c. \quad (2)$$

The corrective factor of 1/4 accounts for:

- since Jupiter reflects the Sun's light, the Doppler shift occurs twice, once when the starlight hits the planet, and again when the reflected light leaves its surface;
- the measurement considers both edges of the planetary disk together.

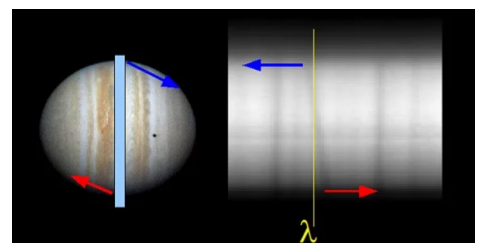


Figure 2: Schematic representation of the method used to calculate Jupiter's rotational period from spectroscopic observations. *Left*: the thick line indicates the orientation of the spectrograph slit across the planetary disk, while the two arrows represent the tangential velocities at the approaching and receding edges of the planet. *Right*: the corresponding spectrum of Jupiter, where the Doppler-induced tilt in a spectral line is clearly visible. [11]

3 Instrumental set-up

The instrumental setup used for data collection consists of several key components:

- A Schmidt-Cassegrain telescope with a 280 mm aperture and a focal ratio of f/10, equipped with an

²Otherwise, the line-of-sight angle would need to be taken into account.

f/6.3 focal reducer. The system includes automatic alignment and pointing capabilities, performed using the All-Star Polar Alignment software [7]. The telescope has an equatorial mount;

- A Lhires III spectrograph, designed for high-resolution spectroscopic observations;
- A CCD camera (ATIK 460EX), whose specifications are listed in Table 1;
- A laptop computer running the Maxim DL software, used to control the CCD camera and manage data acquisition.

Table 1: CCD camera ATIK 460EX specifications. [5]

Specification	Value
Horizontal Resolution	2750 pixels
Vertical Resolution	2200 pixels
Pixel Size	4.54 μm x 4.54 μm
Sensor Size	12.5 mm x 10 mm
ADC (Analog-to-Digital Converter)	16 bit
Binning	2x2
Readout Noise	5e- typical value
Gain Factor	0.27e-/ADU
Dark Current	$\sim 0.0004 \text{ e-}/\text{s}$ at -10°
Power Supply	12V
Maximum Exposure Time	Unlimited
Minimum Exposure Time	1/1000 s
Cooling	Yes ($\Delta T = -25^\circ\text{C}$)
Backfocus Distance	13 mm
Telescope Connection	T-thread Female (42x0.75)
Weight	400 g

3.1 The Lhires III

The Lhires III (Littrow High Resolution Spectrograph) is a spectrograph optimized for high-resolution spectroscopy using amateur-sized telescopes. A schematic representation of the spectrograph is shown in Fig. 3. In a Littrow-mounted spectrograph the same optical component, in this case a 200 mm lens, acts as both the collimator to render the light beam parallel, and the focusing (or imaging) lens to bring a focused image of the spectrum onto the detector. This design eliminates the need for separate lenses for collimating and focusing, making the Lhires III more compact. The usable field over which the spectrum is obtained has been deliberately restricted to allow the use of a simple achromatic doublet as the objective lens. This design choice reduces chromatic and spherical aberrations, ensuring a better optical performance.

The entrance slit of the spectrograph is highly polished and inclined at 10° to the optical axis of the telescope. This polished surface acts as a mirror for light from objects that do not pass through the slit, reflecting it back to a guide camera. This arrangement enables the alignment of the slit with the target object (see Fig. 4).

The light from the telescope passing through the slit is directed by a flat 45° mirror to the collimator lens (focal length: 200 mm; diameter: 30 mm). The resulting collimated beam is then directed to a plane reflection grating, which is mounted on a pivoting support. By rotating the grating via a precision micrometer screw, we can select different spectral ranges. The spectrograph is equipped with multiple interchangeable reflection gratings, allowing to choose the optimal balance between spectral resolution

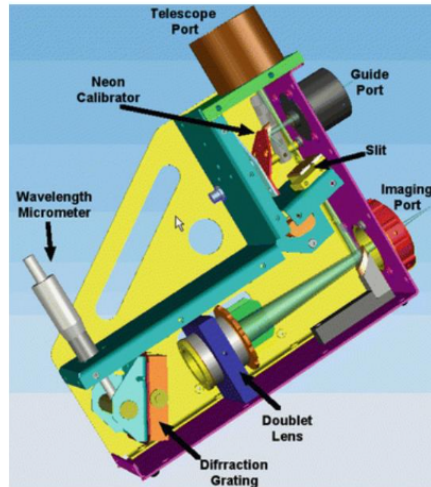


Figure 3: Schematic representation of the Lhires III spectrograph. The main components are highlighted in the figure.

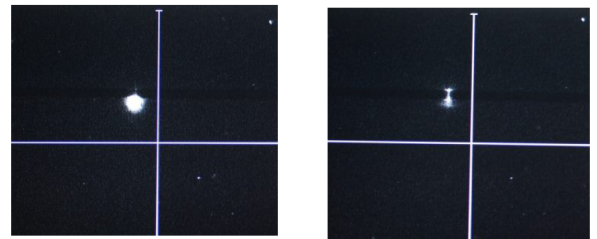


Figure 4: Example of slit orientation using the guiding camera. The entrance slit is just perceptible as a darker horizontal line against the slightly brighter sky background. On the left, the star is not on the slit. On the right, it is correctly positioned on the slit. The star's intensity has been strongly reduced since most of the light is now passing through the spectrograph. [11]

and limiting magnitude. The specifications of the Lhires III spectrograph are listed in Table 2. For the purposes of this study, a 1200 lines/mm grating was used. Finally, the dispersed light from the grating passes back through the lens and is focused on the detector.

Lhires III is also equipped with a Ne/Ar lamp that can be used to perform wavelength calibration.

4 Observation and Data Collection

The observation was conducted in Pisa, at the Department of Physics “Enrico Fermi” of the University of Pisa. It began on 2024-11-05 at 19:15:49 UTC and ended at 20:16:19 UTC. The telescope was previously mounted and aligned by faculty members. During the session, a spectroscopy system was set up using a CCD camera and an adapter to capture the spectrum via a diffraction grating. The setup process began with the installation of the CCD camera adapter, followed by the insertion of the Lhires III core element into the adapter body. The camera was then manually focused to clearly observe the slit and ensure the spectrum was properly focused. If necessary, the focus was fine-tuned by rotating the CCD camera adapter body while acquiring a series of images to monitor and improve the focus quality.

Once the acquisition camera had been set up and properly focused, a spectrum of the internal Neon-Argon calibration lamp in the Lhires III was acquired. Using the micrometer screw, the diffraction grating angle was adjusted to a region containing prominent Neon emission

Table 2: Spectrograph performance for different Lhires III gratings. [11]

	Grating – Lhires III (lines/mm)				
	2400	1200	600	300	150
Dispersion ($H\alpha$) [nm/pix]	0.012	0.035	0.074	0.149	0.300
Resolving power	17000	5900	2800	1400	700
Field of view [nm]	8.5	25	55	110	230
Limiting magnitude	5.0	6.8	7.5	8.4	9.2

lines, specifically near the Na I doublet, where the lamp exhibits two well-known reference lines. Then, the Neon lamp was turned off and removed from the slit entrance by rotating the corresponding control knob. The telescope was then pointed at the target object, and the slit was centered on the source using the guiding camera. For observations of Jupiter, the slit was aligned along the planet’s equator to capture the region exhibiting the highest rotational velocity. Since achieving perfect alignment is challenging, the CCD camera orientation was subsequently adjusted to ensure the spectral trace was aligned with the horizontal axis of the image. Finally, we also acquired calibration frames.

At the end of the observation session, the following data were collected:

- three exposures of Jupiter with an exposure time of 30 seconds each;
- two lamp spectra with an exposure time of 30 seconds, taken immediately after the Jupiter exposures;
- one flat field with an exposure time of 10 seconds;
- three exposures of Vega with an exposure time of 30 seconds each;
- two lamp spectra with an exposure time of 30 seconds, taken immediately after the Vega exposures;
- one flat field with an exposure time of 20 seconds;
- five dark frames with an exposure time of 30 seconds (matching the exposure time of the scientific frames);
- ten bias frames.

5 Data Reduction and Results

Based on the data acquired during the observation, image processing and examination were carried out to fulfill the primary objectives of the experiment: to measure the spectrum of Vega and to determine Jupiter’s rotation period through spectroscopic analysis. The data reduction and analysis followed the steps outlined below:

- First of all, the pre-processing of the scientific images was performed by subtracting the *master bias* and *master dark* frames and dividing by the *normalized flat field*;
- The spectra were then rotated to align them with the *x-axis* of the image;
- The sky background was analyzed;

- The spectra were extracted from the astronomical images of Jupiter, Vega, and the calibration lamps, resulting in one-dimensional spectra;
- Wavelength calibration was performed;
- Based on the lamp spectra, the resolving power of the instrument was determined along with the binning error in order to estimate the uncertainty on the measured line positions;
- The spectrum of Vega was analyzed and the sodium doublet lines were identified;
- Finally, Jupiter’s spectrum was analyzed, and its rotation period was calculated from the Doppler shift of the spectral lines.

5.1 Spectrum Reduction

Photons emitted by the astronomical source are collected by the CCD sensor and converted into an electrical signal, which is read out at the end of the exposure. The read-out process produces a matrix of counts corresponding to the various positions on the CCD, described by the function $ADU(x, y)$ (*Analog-to-Digital Units*), and stored on a computer in a FITS file that can be displayed as an image. This matrix does not directly represent the intrinsic signal $I(x, y)$ from the astronomical object, and a calibration of the images is required. In fact, the measured signal consists of several contributing components:

$$ADU(x, y) = I(x, y) \times FF(x, y) + BIAS(x, y) + DARK(x, y) \quad (3)$$

where:

- $I(x, y)$ represents the light flux incident on the CCD;
- $FF(x, y)$ (*Flat field*) accounts for the pixel-to-pixel sensitivity variation across the CCD. In an ideal detector, the response to a uniformly illuminated field would be constant over the entire sensor. In practice, non-uniformities in the sensitivity lead to systematic errors in photon counts;
- $DARK(x, y)$ corresponds to the dark current, which arises from thermally generated electrons within the CCD. To reduce this source of noise, the CCD is kept at a low temperature using a cooling system. Dark frames must be corrected by subtracting the bias signal;
- $BIAS(x, y)$ represents the zero-level offset added during the readout process and allows for the estimation of the CCD readout noise. It is measured by taking very short exposures (ideally with zero

exposure time) with the shutter closed, so that no photons or thermal electrons are recorded. The resulting distribution of pixel values centers around the nominal zero level. To avoid negative pixel values during readout, a baseline voltage is intentionally added to all images. Therefore, the bias frame must be subtracted from the scientific images during the data reduction process.

By inverting Eq. 3, the intrinsic intensity of the source can be obtained as:

$$I(x, y) = \frac{ADU(x, y) - BIAS(x, y) - DARK(x, y)}{FF(x, y)}. \quad (4)$$

We then proceeded with the image reduction process. First, the bias frames were combined using a sigma-clipping algorithm to exclude outliers. The median was used as the central estimator, and the standard deviation was estimated using the Median Absolute Deviation (MAD)

$$MAD = \text{median}(|x_i - \tilde{x}|) \quad (5)$$

where $\tilde{x} = \text{median}(x)$. We used a reasonable MAD of 3σ . The remaining pixel values were averaged across all frames³ to obtain the *master bias*, which was subsequently subtracted from all other exposures. In the same way, the dark frames were combined to produce the *master dark*. Since the flat fields for Vega and Jupiter were acquired with different exposure times, we used only the flat field associated with Vega to construct the *master flat*, shown in Fig. 5. As we can see in the image, a portion of the CCD remains unilluminated. This unilluminated region is present in all scientific exposures, including the Vega and Jupiter spectra as well as the lamp frames. Consequently, all images were trimmed to exclude this region. The *master flat* was then normalized to generate the *normalized master flat*, reported in Fig. 5. Dust and grain artifacts appear as dark spots in the image, indicating inhomogeneities in the CCD or optical path. Finally, we processed all the scientific images using Eq. 4. An example of a Vega spectrum before and after preprocessing is shown in Fig. 6.

5.2 Spectral Alignment

Although the spectrograph slit is ideally aligned such that the dispersion direction is perfectly parallel to the *x-axis* of the CCD, in practice this is not always the case. Therefore, it is necessary to rotate the spectral images before performing wavelength calibration.

To quantify the misalignment, we analyzed the spectra of both Vega and Jupiter, dividing each image into 55 equally spaced sections along the dispersion axis (so with a step of 50 rows). For each section, we determined the peak position in the cross-dispersion direction (*y-axis*), using the FWHM as an estimate of the uncertainty on the peak position. These peak positions were then fitted with a straight line, and the slope of the fit was used to calculate the rotation angle required to align the spectrum with the CCD axes. Figure 17 in the App. A shows some examples of fits and images of Vega and Jupiter before and

³That reduces the noise of the image by a factor $1/\sqrt{n}$, with n the number of images combined

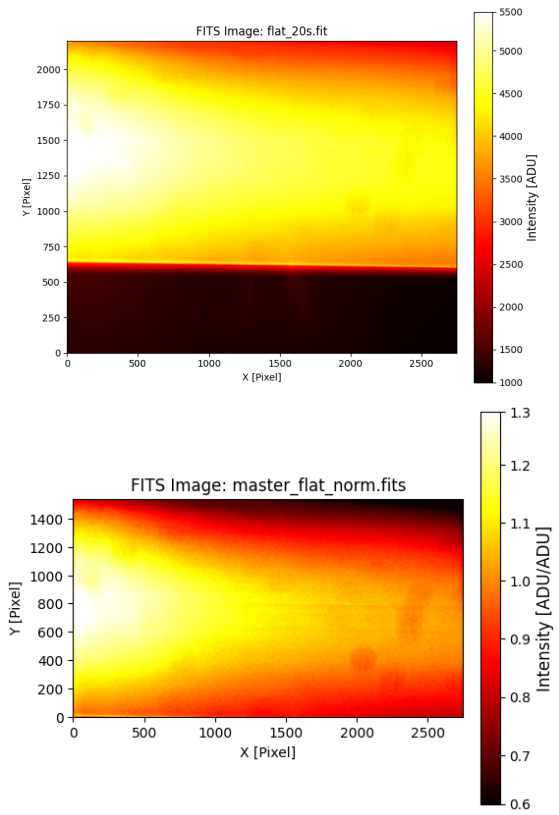


Figure 5: Flat Fields. *Top*: Raw flat field image. A non-illuminated region is clearly visible at the bottom of the frame. *Bottom*: Normalized master flat field, obtained after subtracting the *master bias* and trimming the image to exclude the unilluminated area. Several dark spots are visible, which are attributed to dust particles on the optical path or the CCD surface.

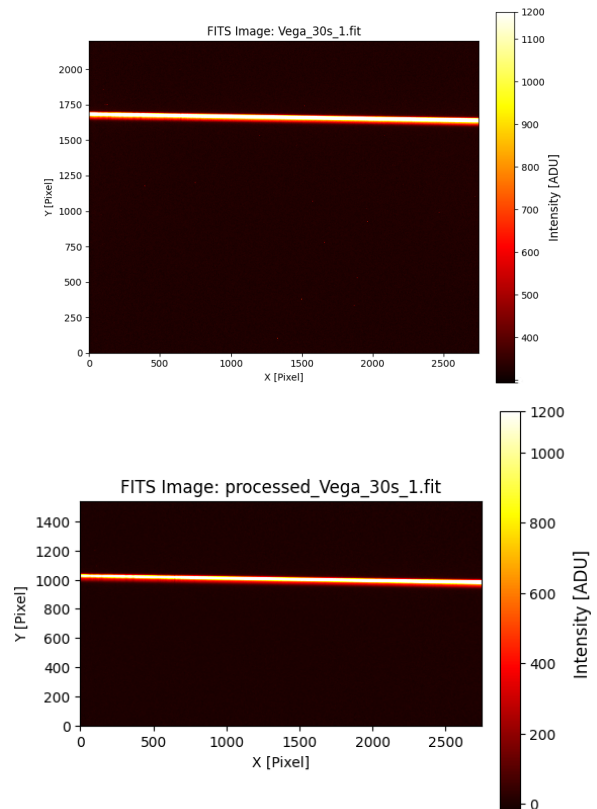


Figure 6: Vega Spectrum Before and After Preprocessing. *Top*: Raw spectrum of Vega prior to preprocessing. *Bottom*: Processed spectrum after bias and dark frames subtraction, and flat-field correction.

after rotation. We can see that a linear fit is sufficient to correctly align the spectra. In Table 3 the fit parameters obtained for each image are reported.

Finally, the lamp images corresponding to each target (Vega and Jupiter) were also rotated using the same angles determined from the fits. We applied the angle obtained from the last image in each dataset, since the lamp images were taken after the last target exposures. In Fig. 18 in the App. A a lamp image before and after the rotation is reported.

Table 3: Parameters obtained from the linear fit applied to the peaks identified in the spectra of Vega and Jupiter (see Fig. 17 in Appendix A).

Image	Angle ($^{\circ}$)	Err ($^{\circ}$)
Vega_30s_1	0.94	0.02
Vega_30s_2	0.89	0.02
Vega_30s_3	0.90	0.01
giove_30s	0.70	0.11
giove_30s_1	0.95	0.09
giove_30s_2	0.94	0.09

5.3 Sky subtraction

In spectroscopic images, in addition to the source, the sky background is also recorded. This background consists in diffuse light and spectral lines originating from elements present in the Earth atmosphere. Unlike the lines from the astronomical source, these atmospheric lines appear straight, as the atmosphere is stationary compared to us. The sky background must be subtracted from the image. To do this, a region containing only sky, i.e., without signal, near the spectrum was selected and its mean value was computed. The resulting background counts were found to be very low (on the order of 10) compared to the source signal (on the order of 10^3), making the subtraction unnecessary in this case.

5.4 Spectrum extraction

As we can see in Fig. 7, it was necessary to identify the region of the image containing the spectrum before proceeding with spectral extraction. This was accomplished using the trace method. Similar to the approach described in Sec. 5.2, for each column of the image we identified the maximum peak intensity and the corresponding FWHM using the `find_peaks` function, with a minimum width threshold set to exclude isolated points that do not correspond to the actual spectrum. The results were then plotted and, after removing any outliers, we fitted the peak positions with a polynomial function. For the images analyzed, a first-degree polynomial function was sufficient. The resulting lines, since the images had already been rotated, corresponded as expected to horizontal lines. Therefore we took the intercept as the central value of the spectrum. The mean FWHM of the valid points was then computed and used to define the upper and lower bounds of the spectral region. An example is shown in Fig. 7. The images were then trimmed to include only the identified spectral region and eliminate borders.

To reduce noise, the first and second spectra of Vega were combined. The third spectrum was excluded from

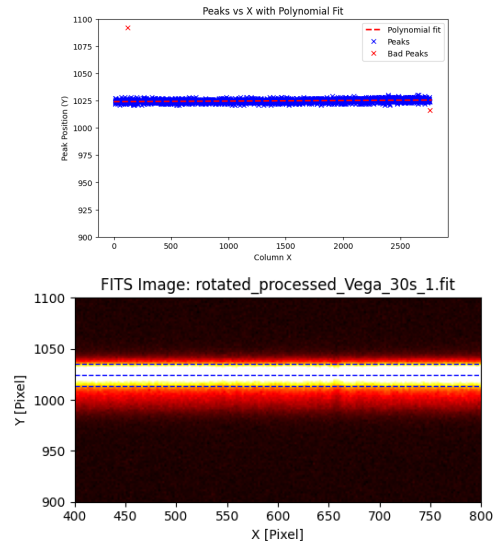


Figure 7: Extraction of Vega spectrum. *Top*: Detected peaks in the spectrum. Outliers are marked with red crosses, while the fitted line is shown as a red dashed line. *Bottom*: Region containing the spectrum. The central value is 1024.1 ± 0.1 , with an upper bound of 1034.9 ± 0.6 and a lower bound of 1014.1 ± 0.6 . We can observe a diffuse halo surrounding the spectrum, which is attributable to atmospheric effects such as seeing, as well as to imperfections in the optical system.

the analysis, as it exhibited significantly fewer counts compared to the other two. The spectra of Jupiter were not combined, since the tracing procedure identified significantly different dimensions for the spectral region across the three images. Therefore, only the first spectrum was used, as it presented better-defined sodium lines.

Finally, an average along the image columns was performed to obtain the final one-dimensional spectrum.

For the lamp spectra, we directly trimmed the exposures to eliminate borders and combined them for Vega and Jupiter, and then performed an average along the columns to extract the spectrum. Since the lamp spectrum extends across the entire image rather than being confined to a specific region, the trace operation was not required.

5.5 Wavelength Calibration

The purpose of the wavelength calibration procedure is to convert the pixel values along the dispersion axis into physical units of wavelength (\AA). To achieve this, we analyzed our lamp spectra and compared them with a reference spectrum of a Ne/Ar calibration lamp available from the NOIRLab (National Optical-Infrared Astronomy Research Laboratory) Spectral Atlas [2]. We identified the emission lines listed in Table 4. These lines were then plotted in a wavelength versus pixel graph, and the points were fitted with a polynomial function to establish a mapping from pixel positions to wavelengths. We tested first-, second-, and third-degree polynomial fits, selecting the best model based on the reduced chi-squared. The second-degree polynomial provided the best fit and was therefore adopted for the pixel-to-wavelength calibration. This polynomial was then used to calibrate our lamp spectra. Fig. 8 shows the calibrated lamp spectra for both the Vega and Jupiter lamps, including the identified emission lines and the corresponding residuals. The standard deviation of the residuals was taken as the uncertainty in the line position: for the Vega spectrum a standard deviation

Table 4: Identified spectral lines with known wavelength and corresponding pixel position for Vega and Jupiter lamps.

Wavelengths [Å]	Atom	Corresponding Pixel (Lamp Vega)	Corresponding Pixel (Lamp Jupiter)
5944.8342	NeI	98	85
5928.8130	ArI	254	241
5912.0853	ArI	416	403
5888.5841	ArI	644	631
5881.8950	NeI	708	695
5852.4878	NeI	989	977
5820.1558	NeI	1302	1289
5764.4188	NeI	1834	1821

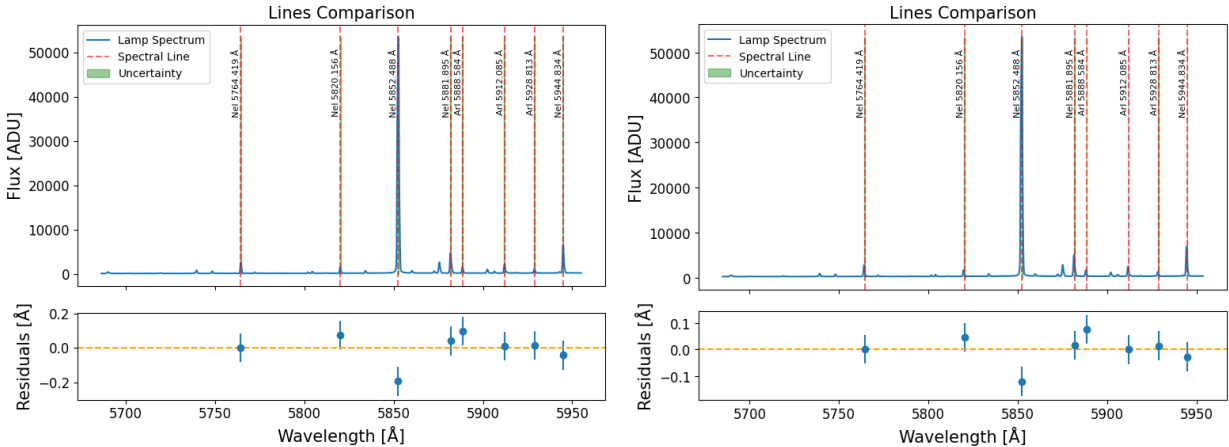


Figure 8: Calibrated spectrum of the Vega lamp (*left*) and the Jupiter lamp (*right*). The graphs show the lamp spectra, with wavelength in Angstrom on the x-axis and intensity in ADU (Analog-to-Digital Units) on the y-axis. Known emission lines are indicated by vertical dashed lines. Residuals from the wavelength calibration fit are displayed in the bottom panel.

of 0.084 \AA was found, while for the Jupiter spectrum a standard deviation of 0.054 \AA was found.

5.6 Spectral Resolution and binning error

A key parameter characterizing the ability of a spectrograph to resolve spectral features that are closely spaced in wavelength is the spectral resolution, defined as

$$R = \frac{\lambda}{\delta\lambda}, \quad (6)$$

where $\delta\lambda$ represents the spectral purity, i.e., the ability of the spectrograph to distinguish fine details in the spectrum. The resolution can be empirically determined by measuring the full width at half maximum of emission lines in a lamp spectrum and assuming $\delta\lambda \sim FWHM$. For this purpose, we selected two unsaturated, isolated, and strong emission lines (NeI 5889 Å and NeI 5892 Å) in the Vega and Jupiter lamp spectra. These lines were chosen specifically because the NaI doublet wavelengths are comprehended in this range, which will be analyzed in the following sections. A Gaussian function plus a constant offset to model the continuum was fitted to each line to derive the central wavelength and the FWHM from the standard deviation σ using the relation

$$FWHM \approx 2.355 \sigma. \quad (7)$$

For each line, the number of bins was also calculated by considering an effective width of the line of 5σ . We then computed the spectral resolution R for each line and calculated the mean value. The results of the Gaussian fits are shown in Fig. 9 and summarized in Tab. 5. We obtained a mean spectral resolution of $R = (6.711 \pm 0.096) \times$

10^3 for the Vega lamp and $R = (7.10 \pm 0.10) \times 10^3$ for the Jupiter lamp.

Subsequently, based on the fit results, we calculated the binning error associated with each spectral line using the following formula

$$\sigma_{bin} \sim \frac{FWHM}{\sqrt{N}} \quad (8)$$

where N is the number of bins in the line. This expression is valid under the assumption that each bin is statistically independent. This uncertainty represents the error on the line positions measured in the spectra of Vega and Jupiter, and it accounts for instrumental broadening effects. The results are reported in Table 5. We notice that the number of bins obtained for each line is the same in the Vega and Jupiter lamp spectra separately. For Vega, we obtained $\sigma_{bin} = 0.15$ while for Jupiter $\sigma_{bin} = 0.14$.

5.7 Spectral analysis of Vega

Fig. 10 shows the extracted spectrum of Vega after wavelength calibration. By comparing our spectrum with that reported in the literature and shown in Fig. 11, we can identify the NaI absorption lines. The positions of the NaI doublet are indicated by dash-dotted vertical lines in our spectrum reported in Fig. 10. As we can see, the spectrum exhibits a strong absorption feature corresponding to the NaI D2 line. The NaI D1 line cannot be identified, as it is weaker and indistinguishable from the noise. The H_2O (5919 Å and 5924 Å) due to the terrestrial atmosphere are also visible.

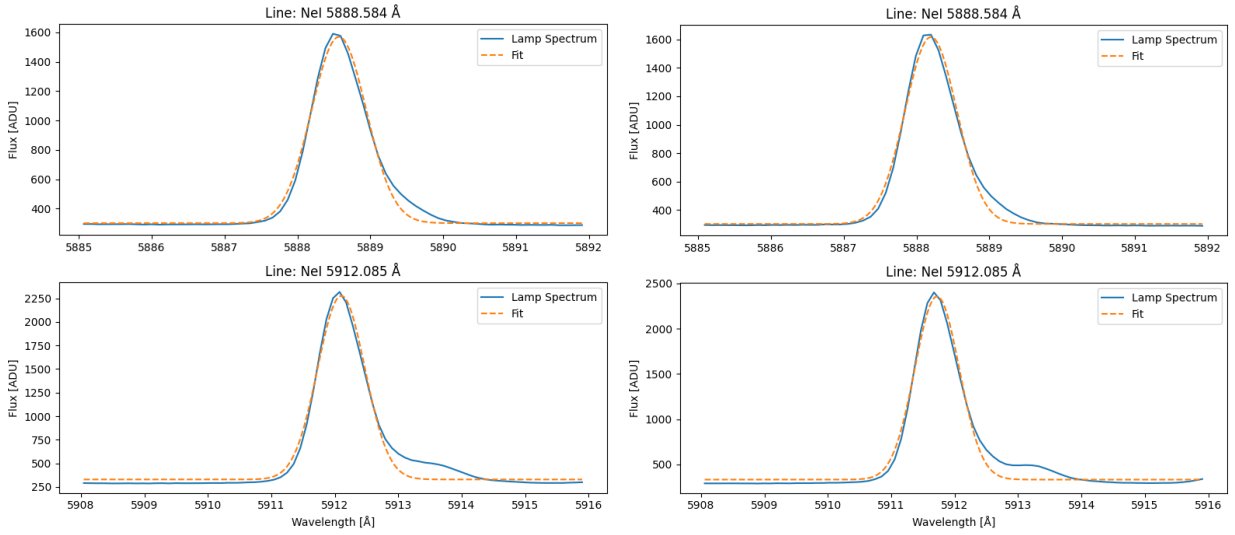


Figure 9: Gaussian fit for the NeI lines at 5888.584 Å and 5912.085 Å in the Vega lamp spectrum (*left*) and in the Jupiter lamp spectrum (*right*).

Table 5: Measurements for the Vega and Jupiter lamps. The measured wavelength, the FWHM, the resolving power, the number of bins and the binning error are reported for each line with the corresponding uncertainty.

Vega Lamp							
Measured λ (Å)	λ err (Å)	FWHM (Å)	FWHM err (Å)	R	R err	N_{bins}	σ_{bin}
5888.57	0.01	0.88	0.02	6.67×10^3	0.11×10^3	36	0.15
5912.10	0.01	0.88	0.02	6.76×10^3	0.16×10^3	36	0.15

Jupiter Lamp							
Measured λ (Å)	λ err (Å)	FWHM (Å)	FWHM err (Å)	R	R err	N_{bins}	σ_{bin}
5888.20	0.01	0.84	0.01	7.04×10^3	0.12×10^3	35	0.14
5911.72	0.01	0.82	0.02	7.17×10^3	0.16×10^3	35	0.14

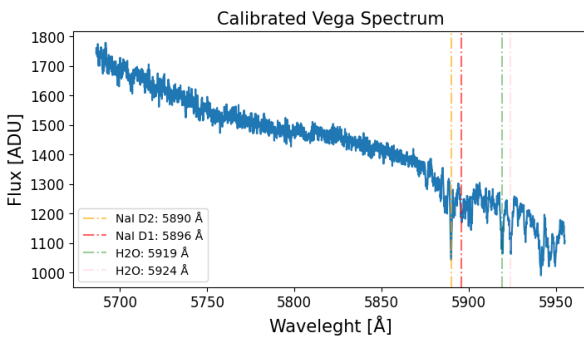


Figure 10: Spectrum of Vega extracted from the combined exposures after wavelength calibration. The absorption lines of the sodium doublet and of the H_2O are shown as dash-dotted lines.

We isolated the regions of the spectrum close to the line and fitted a Voigt profile function plus a constant offset to model the continuum. The results of the fit is summarized in Tab. 6. We then added in quadrature the uncertainties from the wavelength calibration (see Sec. 5.5), the fit uncertainties, and the σ_{bin} (see Sec. 5.6). The resulting value, which was found to be 0.21 Å, was taken as the total error on the measured line position. The dominant source of uncertainty arises from the σ_{bin} of the instrument. Finally, we plotted the fitted line positions and its uncertainty on the Vega spectrum together with the known wavelengths of the NaI doublet. As we can see from Fig. 12, our results are consistent with the expected values.

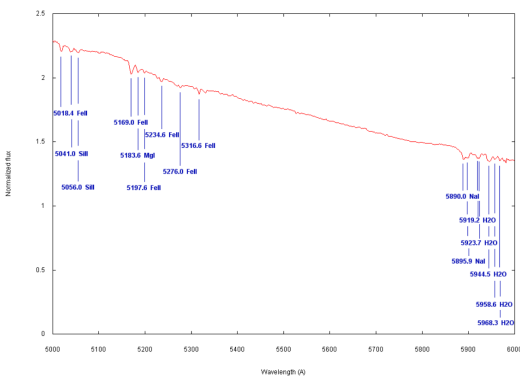


Figure 11: Example of calibrated and normalized spectrum of Vega [3].

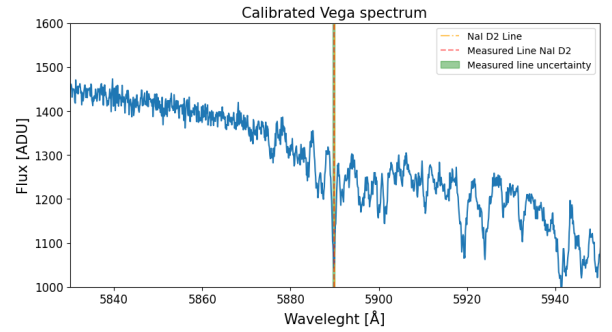


Figure 12: Wavelength-calibrated spectrum of Vega. The NaI D2 emission line of the sodium doublet is shown as orange dash-dotted lines, while the measured line is indicated by red dashed lines. The uncertainty in the line position is represented in green and is equal to 0.21 Å. The dominant source of uncertainty arises from the binning.

Table 6: Fit results for the Voigt profile for the NaI D2 line in Vega spectrum.

Parameter	Value	Uncertainty
Center (λ) [Å]	5889.82	0.03
Sigma (σ) [Å]	0.54	0.09
Lorentzian width (γ) [Å]	0.49	0.23
Offset	1250.0	5.2

5.8 Spectral analysis of Jupiter: radial velocity

Fig. 13 shows the extracted spectrum of Jupiter after wavelength calibration. Again, we can identify the NaI doublet absorption lines which positions are indicated by dash-dotted vertical lines. In this case, both NaI D2 and NaI D1 are visible.

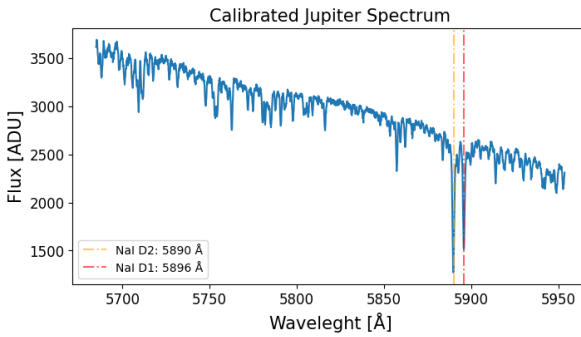


Figure 13: Spectrum of Jupiter extracted after wavelength calibration. The emission lines of the sodium doublet are shown as dash-dotted lines.

The radial velocity of the planet along the line of sight was then calculated from the Doppler shift of the sodium doublet lines. Each of the two lines was analyzed separately, and a Voigt profile plus a constant offset to model the continuum was fitted. The results of the fit are shown in Fig. 14 and summarized in Tab. 7. Based on the fitted line centers, we used the Doppler formula given in Eq. 1, including a correction factor of 1/2 to account for the fact that the light was reflected by the planet, thus the Doppler effect happens twice (see Sec. 2.5). The total uncertainty on the line position was computed by summing in quadrature the errors from the wavelength calibration, the fitting procedure, and the binning error σ_{bin} , which is again the dominant source of error. The radial velocity values obtained from the two lines were averaged, and the corresponding uncertainty was determined through standard error propagation. Finally, we obtained a radial velocity of the planet of (-3.0 ± 2.5) km/s. We note that the velocity is negative, indicating that the object is

approaching the observer.

5.9 Spectral Analysis of Jupiter: Rotational Period

To calculate Jupiter's rotational period, it was first necessary to identify the edges of the planet in the spectrum, as discussed earlier in Sec. 2.5. However, as shown in Fig. 15, which displays a portion of Jupiter's spectrum, the effects of seeing and optics at the spectral extremes are significant, making an accurate determination of the planet's edge imprecise and difficult.

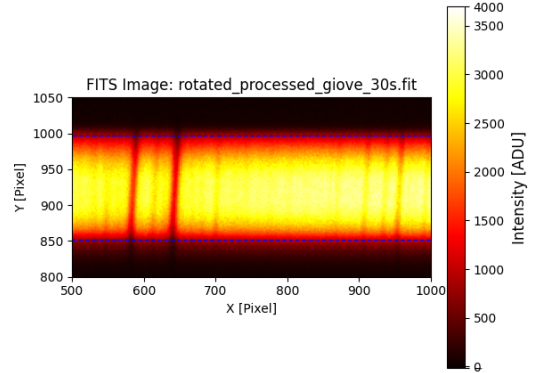


Figure 15: Jupiter spectrum. The blue dashed line represent the bounds for the spectral region considered. The uncertainties are that coming from the fitting procedure.

To proceed with the calculation of the *line tilt*, we assumed that: we are in the limit of large distances, Jupiter rotates as a rigid body, and the slit was perfectly aligned with the planet's equator. Under these assumptions, the velocity is expected to increase linearly with the radius R ($v = \omega R$, with ω the angular velocity), and consequently the tilt of the spectral line (see Eq. 1) is also expected to follow a linear trend and thus be represented by a straight line.

The spectral region was then identified in the image (see Fig. 15), and the regions corresponding to the sodium doublet lines were isolated separately. A Voigt profile plus a constant offset for the continuum was then fitted, for each position along the slit (y-axis), along the dispersion direction. This procedure was iterated over the entire vertical extent of the identified region. At each iteration, the initial guess parameters for the fit were updated using those from the previous iteration, and the fitted central wavelength of the line and its corresponding uncertainty

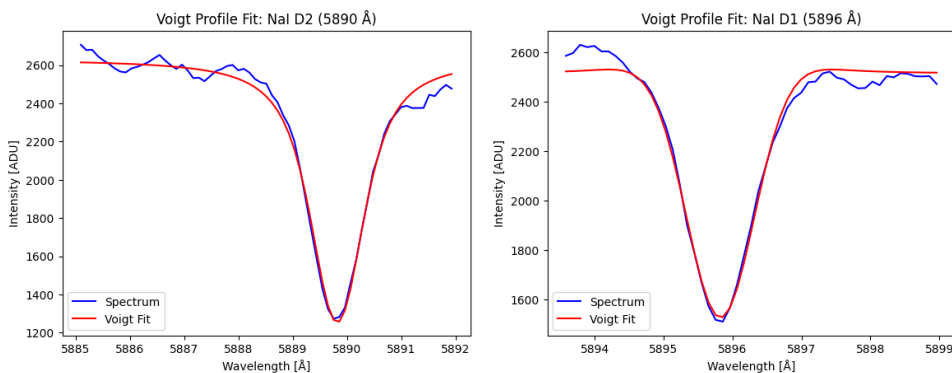


Figure 14: Voigt profile fit with a constant offset to model the continuum for the D2 and D1 sodium lines in Jupiter's spectrum.

Table 7: Fit results of the Voigt profile of the NaI doublet lines in the Jupiter spectrum.

NaI D2 (5890 Å)				
Amplitude (ADU)	Center (Å)	σ (Å)	γ (Å)	Offset
$(-2.36 \pm 0.11) \times 10^3$	5889.82 ± 0.01	0.240 ± 0.052	0.45 ± 0.05	2631 ± 12

NaI D1 (5896 Å)				
Amplitude (ADU)	Center (Å)	σ (Å)	γ (Å)	Offset
$(-109 \pm 11) \times 10^4$	5895.82 ± 0.01	0.52 ± 0.05	-0.12 ± 0.01	2514 ± 16

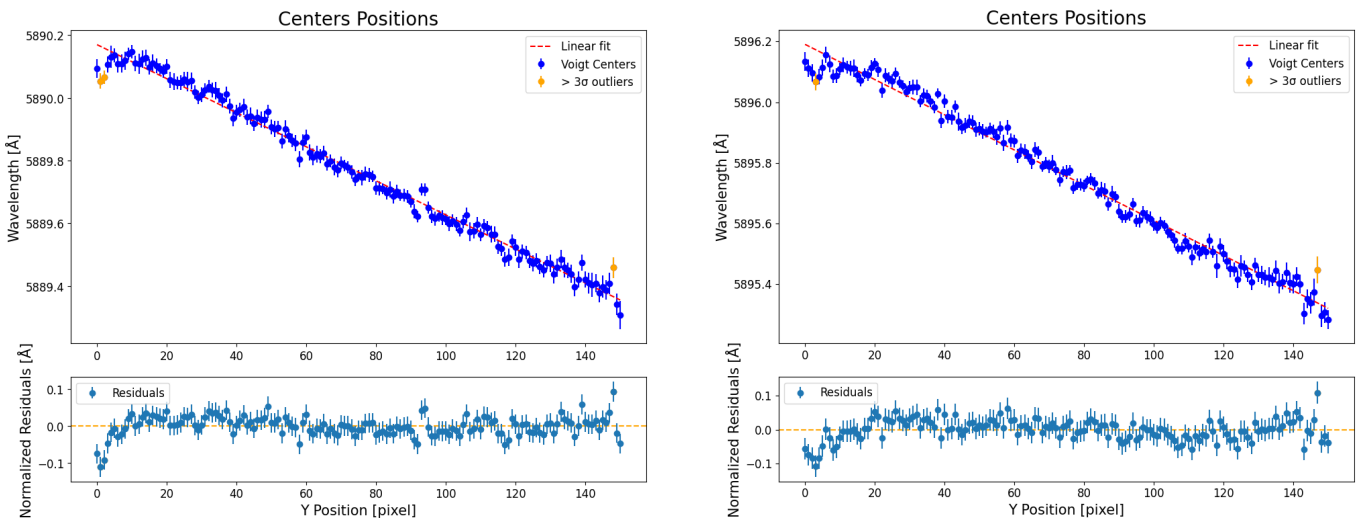


Figure 16: In the top panel, the positions of the spectral line centers obtained at each position along the slit are shown. The NaI D2 line is displayed on the right, while the NaI D1 line is on the left. The linear fit is represented by a red dashed line, and the outliers are highlighted in orange. The bottom panel shows the residuals.

were recorded. Next, the fitted central wavelengths and their associated errors were plotted as a function of the position along the slit and were fitted with a straight line. All points deviating more than 3σ from the fit were excluded, where σ was taken as the standard deviation of the residuals. The results of the line fits and the corresponding residuals are shown in Fig. 16.

The wavelength gradient $\Delta\lambda$ was then calculated. To reduce the influence of edge values affected by instrumental errors and seeing, the first half of the measured values (corresponding to the receding limb of the planet) and the second half (corresponding to the approaching limb) were separately averaged, and the difference between the two averages was taken. To avoid the underestimation of the uncertainty, the binning error σ_{bin} (which is the dominant source of uncertainty) was directly assigned to both averaged values, without propagating the error through the averaging process. The resulting gradient corresponds to half the total *tilt* of the line, since the averaging considered points located halfway between the limb and the center of the planet. Using the Doppler formula in Eq. 2, without taking into account the correction factor $1/2$ (as we no longer consider simultaneously both sides of the planet, see Sec. 2.5), the tangential velocity of the planet was derived from each sodium line and then the two values were averaged. The results are reported in Tab. 8. The average tangential velocity obtained is (11.0 ± 2.5) km/s.

Finally, from the calculated tangential velocity, the angular velocity of the planet was computed by dividing by Jupiter's radius, taken to be $R = 71492$ km (see [4]). We obtained a value of $(1.54 \pm 0.35) \times 10^{-4}$ rad/s, with the uncertainty obtained through standard error propagation. The rotational period P of the planet was then calculated

Table 8: Tilt values and tangential velocities derived for the sodium doublet lines.

Line	$\Delta\lambda$ (Å)	Tangential Velocity (km/s)
NaI D2	0.42 ± 0.14	10.6 ± 3.5
NaI D1	0.45 ± 0.14	11.3 ± 3.5

using the formula:

$$P = \frac{2\pi}{\omega} \quad (9)$$

resulting in a value of 11.4 ± 2.6 hrs (11h 22m 2.18s), with the uncertainty obtained through standard error propagation.

6 Discussion

The NaI doublet lines were correctly identified in both the Vega and Jupiter spectra, in agreement with the literature (see Fig. 10, 11, 13, and Sec. 2.4). However, in the Vega spectrum, the NaI D1 line was indistinguishable from the background, and therefore could not be identified.

The results obtained for the tangential velocity and the rotational period of Jupiter are consistent with the expected values (see Tab. 9) within the calculated uncertainties, although the measured value for the latter deviates by more than one hour from the known value.

Table 9: Jupiter physical parameters [4] and measured values.

Jupiter physical parameters		Measured
Equatorial radius	71,492 km	
Equatorial rotation velocity	12.6 km/s	11.0 ± 2.5 km/s
Length of day	9.9258 hrs	11.4 ± 2.6 hrs

During the data analysis, the possible sources of error were examined in detail, revealing that the dominant contribution originates from the binning error associated with the instrument itself. This uncertainty inevitably propagated to the measurement of spectral line positions, resulting in relatively high uncertainties in the derived velocities from the Doppler effect. To reduce these uncertainties, both sodium lines in Jupiter's spectrum were considered simultaneously, and the measured velocities were averaged. This approach allowed to reduce the error on the tangential velocity to 22%, compared to 33% when using individual lines. Regarding the radial velocity of the planet, the error amounts to approximately 80%, due to the small magnitude of the measured velocity.

Additional difficulties arose from the quality of the spectral images. In particular, instrumental effects and atmospheric seeing (especially because the observations were made when Jupiter was low on the horizon, so the *seeing*, the artificial light pollution and the contribution of Earth's albedo were stronger) made it difficult to identify the edges of the planet in the images. To address this issue, the method described in Sec. 5.9 was adopted. This approach helped mitigate edge-related distortions and enabled the determination of the spectral line tilt, yielding a result compatible with the known data.

Another source of error affecting the calculation of the equatorial rotational velocity is the alignment of the slit. Although in this experience we assumed that the slit was perfectly aligned with the planet's equator, in practice such alignment is difficult to achieve, and it is never perfect. This introduces a systematic error into the measurement. An additional difficulty arises from the motion of the object itself, which shifts across the sky during the

night, requiring periodic realignment of the slit.

7 Conclusion

The objectives of the experiment were successfully achieved. A complete image processing and reduction procedure was developed, allowing for the extraction and accurate wavelength calibration of the spectra of Vega and Jupiter. The resulting spectra were compared with reference spectra from the literature and found to be consistent. The sodium doublet lines (5890 \AA and 5896 \AA) were identified and measured in Jupiter's spectrum, while in the case of Vega only the D2 line was distinguishable. In addition, the absorption lines at 5919 \AA and 5924 \AA of the H_2O , originating from the Earth's atmosphere, were identified.

From the analysis of Jupiter's spectrum, we inferred an equatorial rotational velocity of $(11.0 \pm 2.5) \text{ km/s}$, from which a rotational period of (11.4 ± 2.6) hours was derived. These values are in agreement with those reported in the literature. The radial velocity of the planet was estimated to be $(-3.0 \pm 2.5) \text{ km/s}$, where the negative value indicates that Jupiter is moving toward the observer. However, the high relative uncertainty ($\sim 80\%$) does not allow us to infer statistically significant physical properties.

Throughout the experience, the main sources of uncertainty were discussed, which are the wavelength calibration, the Voigt profile fitting, and binning errors. The latter was identified as the dominant source of uncertainty, leading to significant errors in the measurements. These were reduced by averaging the velocity values obtained from multiple spectral lines. The main limitations of the instrument, as well as the observational problems that led to image degradation, were also analyzed and discussed.

A Figures

In Fig. 17 and Fig. 18 the spectral alignment process of some exposures is reported.

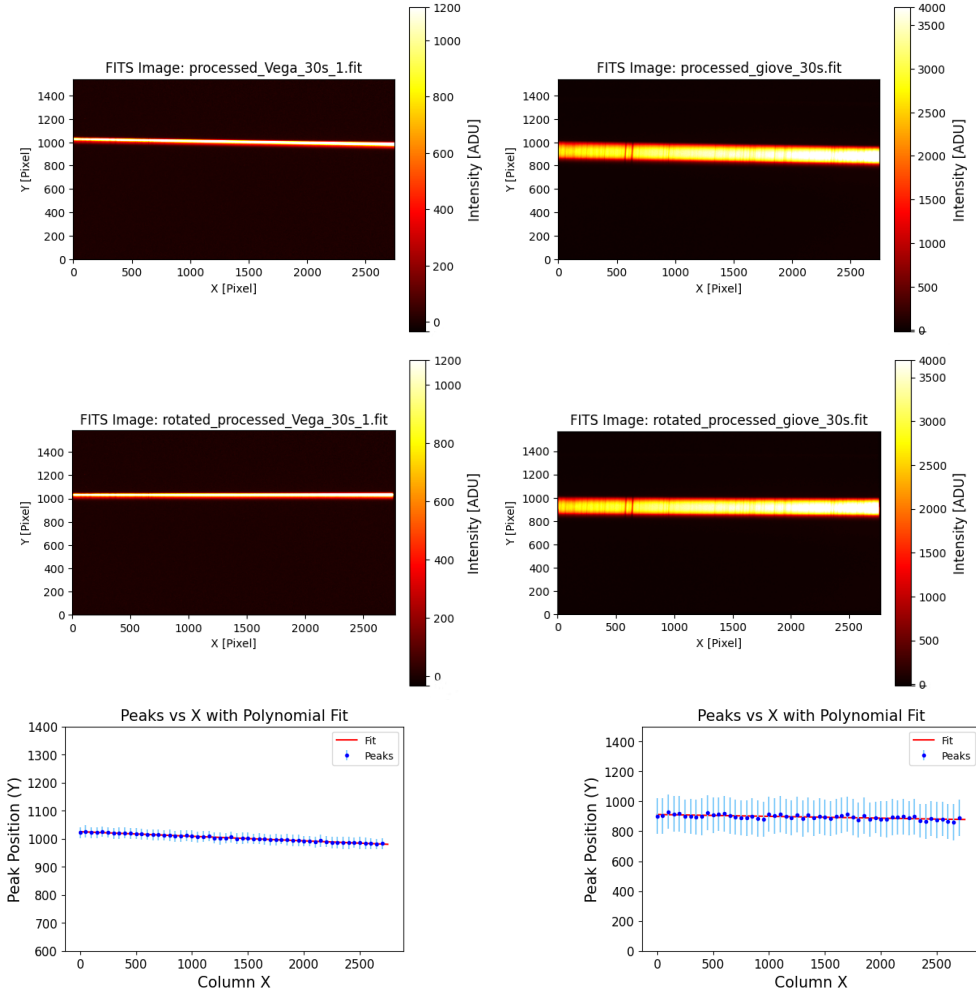


Figure 17: The figure shows the spectral images before and after rotation, along with the linear fit used to determine the rotation angle. The first column displays the images corresponding to Vega, while the second column shows those related to Jupiter.

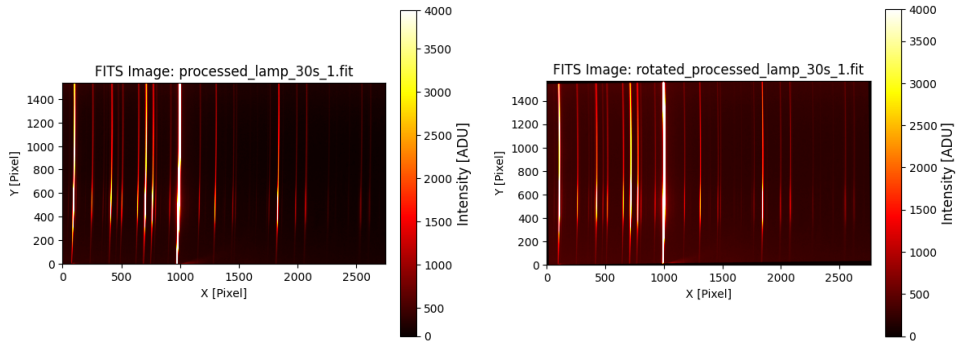


Figure 18: Lamp spectrum before and after rotation.

References

- [1] URL: <https://www.shelyak.com/planets-rotation/?lang=en>.
- [2] URL: https://noirlab.edu/science/data-services/other/spectral-atlas?utm_source.
- [3] URL: <https://buil.astrosurf.com/us/vatlas/vatlas.htm>.
- [4] URL: <https://en.wikipedia.org/wiki/Jupiter>.
- [5] *Atik Series 4 User Manual*. 2012. URL: <https://www.atik-cameras.com/wp-content/uploads/2014/08/AtikSeries4Manual.pdf>.
- [6] Fabio Bresolin. *Astronomical Spectroscopy*. 2022.
- [7] *Celestron: All-Star Polar Alignment*. URL: <https://www.celestron.com/pages/all-star-polar-alignment?srsltid=AfmBOoq6Z-FXrs7gjqgMDnwb5v2rtDwO%5C-CELxm5eiOZuHjjLMTFhgxfmfn>.
- [8] *Celestron: guide to polar alignment with EQ mount*. URL: <https://www.celestron.com/blogs/knowledge%5C-base/how-do-you-polar-align-using-an-eq-mount>.
- [9] Stefano Ciroi and Valentina Cracco. *Dispense di laboratorio di astronomia*. Dipartimento di Fisica e Astronomia, Università degli Studi di Padova, 2015.
- [10] Hannu Karttunen et al. *Fundamental Astronomy*. 5th ed. Springer, 2007.
- [11] Olivier Thizy and François Cochard. *Lhires III – User Guide (English)*. 2006. URL: https://www.astroshop.eu/Produktdownloads/50969_User%20%5C-Guide_English.pdf.